

## Valley-Selective Phonon-Magnon Scattering in Magnetoelastic Superlattices

Liyang Liao<sup>1</sup>, Jorge Puebla<sup>2,\*</sup>, Kei Yamamoto<sup>3,2</sup>, Junyeon Kim<sup>2</sup>, Sadamichi Maekawa<sup>2,3,5</sup>,  
Yunyoung Hwang<sup>1,2</sup>, You Ba<sup>2</sup>, and Yoshichika Otani<sup>1,2,4,†</sup>

<sup>1</sup>*Institute for Solid State Physics, University of Tokyo, Kashiwa 277-8581, Japan*

<sup>2</sup>*Center for Emergent Matter Science, RIKEN, Wako, Saitama 351-0198, Japan*

<sup>3</sup>*Advanced Science Research Center, Japan Atomic Energy Agency, Tokai 319-1195, Japan*

<sup>4</sup>*Trans-scale Quantum Science Institute, University of Tokyo, Tokyo 113-8654, Japan*

<sup>5</sup>*Kavli Institute for Theoretical Sciences, University of Chinese Academy of Sciences, Beijing 100190, China*

 (Received 29 May 2023; accepted 6 September 2023; published 23 October 2023)

Phonons and magnons are engineered by periodic potential landscapes in phononic and magnonic crystals, and their combined studies may enable valley phonon transport tunable by the magnetic field. Through nonreciprocal surface acoustic wave transmission, we demonstrate valley-selective phonon-magnon scattering in magnetoelastic superlattices. The lattice symmetry and the out-of-plane magnetization component control the sign of nonreciprocity. The phonons in the valleys play a crucial role in generating nonreciprocal transmission by inducing circularly polarized strains that couple with the magnons. The transmission spectra show a nonreciprocity peak near a transmission gap, matching the phononic band structure. Our results open the way for manipulating valley phonon transport through periodically varying magnon-phonon coupling.

DOI: [10.1103/PhysRevLett.131.176701](https://doi.org/10.1103/PhysRevLett.131.176701)

Periodic potential landscapes can modify the coupling between two quasiparticles, leading to various emergent phenomena. For example, moiré superlattices can support superconducting [1,2] or quantum anomalous Hall states [3,4] by coupling two layers and forming entangled spin and valley. Bosonic excitations, such as phonons and magnons, are important quasiparticles in solids and have inherent coupling [5–8]. The band structure and wave function of phonons and magnons can be tailored by periodic landscapes in phononic [9–12] and magnonic crystals [13–16]. Similar to the electronic valleys in transition metal dichalcogenide [17,18], honeycomb phononic crystals also have the valley degrees of freedom [19,20]. With the broken inversion symmetry, the phononic valley Hall effect [20] and phononic topological edge states [19,21–23] were observed. Based on magnon-phonon coupling, theoretically, topological chiral phonons have been proposed [24–26]. However, an experimental demonstration of valley phonon transport manipulated by magnon-phonon coupling has yet to be achieved.

Phonons at different valleys are time-reversal pairs. Since magnetism breaks the time-reversal symmetry, magnons may interact differently with the phonons in the two

valleys. As shown in Fig. 1(a), for a honeycomb phononic crystal with sites  $A$  and  $B$  in the unit cell, there is a pair of valleys  $K, K'$  in the Brillouin zone. When the spatial inversion symmetry is broken by inequivalent  $A$  and  $B$

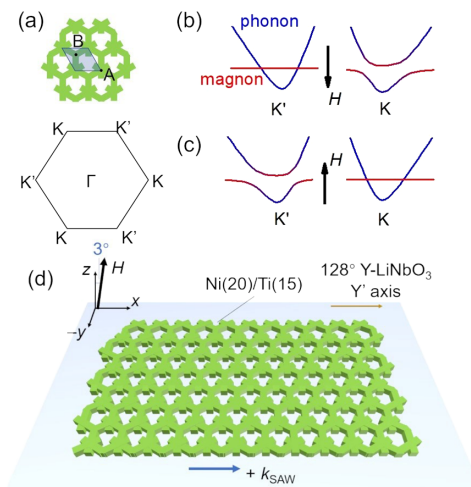


FIG. 1. (a) Unit cell of the honeycomb superlattice and the corresponding Brillouin zone. (b),(c) Schematic of the phonon bands and the magnon bands at the  $K$  and  $K'$  valleys in a symmetry-breaking honeycomb superlattice under an upward magnetic field (b) and a downward magnetic field (c). (d) Honeycomb superlattice made of Ni(20)/Ti(15) in the measurement setup. Magnetic field  $H$  is tilted  $3^\circ$  from the out-of-plane  $z$  direction in the  $xz$  plane, and SAW is excited along the  $Y'$  axis of the  $128^\circ$  YX LiNbO<sub>3</sub> substrate, defined as the  $x$  direction.

Published by the American Physical Society under the terms of the [Creative Commons Attribution 4.0 International license](https://creativecommons.org/licenses/by/4.0/). Further distribution of this work must maintain attribution to the author(s) and the published article's title, journal citation, and DOI.

sites, and an out-of-plane magnetic field component also breaks the time-reversal symmetry, a valley-selective magnon-phonon interaction can emerge, as presented in Figs. 1(b) and 1(c); under a suitable downward magnetic field shifting the magnon energy close to the phonon energy, the phonon in the  $K$  valley interacts with the magnons, while that in the  $K'$  valley does not. The situation reverses when a magnetic field of the same magnitude and opposite direction is applied, with the magnetization in the opposite direction, and the interaction exists only in the  $K'$  valley.

In this Letter, we report the valley-selective phonon-magnon scattering in magnetoelastic superlattices [Fig. 1(d)]. For forward and backward surface acoustic waves (SAW), phonons fall into different valleys and are scattered by the magnetization with different amplitudes, leading to different SAW transmissions, namely nonreciprocal transmission [27,28]. We proposed a circular polarization of the strain field (hereafter strain polarization), which couples with the magnons through magnetoelastic coupling. The strain polarization possesses opposite chirality for the two valleys, resulting in different magnon-phonon coupling strengths, allowing the valley-selective phonon-magnon scattering. Our results demonstrate the manipulation of valley phonon transport via magnon-phonon coupling and provide a new avenue for the coupling between out-of-plane magnetization and SAW [29,30].

We fabricated mirror-symmetry-breaking honeycomb-shaped superlattices using Ni (20 nm)/Ti (15 nm) bilayer film on a  $128^\circ$   $Y$ -cut  $\text{LiNbO}_3$  substrate, as shown in Fig. 1(d). The edge length is 770 nm, and the SAW wavelength corresponding to the  $K$  or  $K'$  point is  $2 \mu\text{m}$ . Details of the superlattice geometry are shown in Supplemental Material (SM), Sec. 1 [31]. The SAW, excited by interdigital transducers (IDT), travels along the substrate  $Y'$ -axis for more efficient hybridization at the valleys (SM, Sec. 2) [31]. While scanning a magnetic field  $H$ , the transmission parameters  $S_{12}/S_{21}$  are measured by a vector network analyzer with a time gating technique. The  $z$  axis is normal to the substrate, and the SAW propagation direction is the  $x$  axis. If not specified, the applied magnetic field is  $3^\circ$  tilted from the out-of-plane  $z$  axis in the  $xz$  plane. Superlattice orientation dependence is studied by patterning rotated superlattices while fixing the SAW propagation direction on the substrate.

Figure 2 shows the transmission measurement results. To compare results in different devices, we normalize the transmission in each device using the transmission at  $\mu_0 H = 0.6$  T, where no magnetization-related SAW absorption exists. In the  $K$ -oriented device (KD),  $+k$  SAW propagates along the  $K$  direction [Fig. 2(a)], whose transmission is represented by  $S_{12}$  (red), and  $-k$  SAW along the  $K'$  direction, represented by  $S_{21}$  (black). The magnetic hysteretic responses are obtained by scanning the external field between 0.6 and  $-0.6$  T. An absorption peak

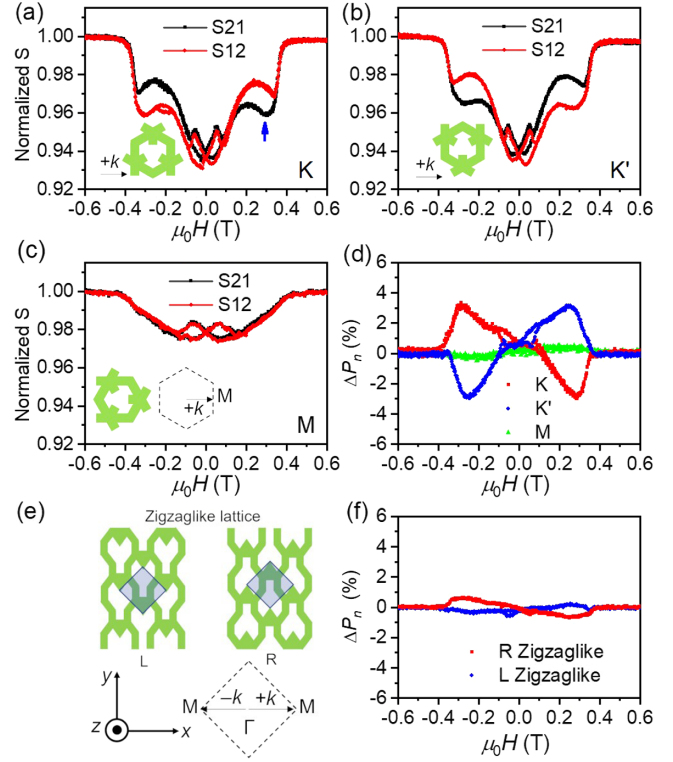


FIG. 2. (a),(c) Normalized transmission parameters  $S_{12}$  (red) and  $S_{21}$  (black) as functions of magnetic field  $\mu_0 H$  for the honeycomb lattice in  $K$ -orientated (a),  $K'$ -orientated (b), and  $M$ -orientated (c) devices. (d) Nonreciprocal absorption  $\Delta P_n = (\Delta P_+ - \Delta P_-)/P$  as a function of magnetic field  $\mu_0 H$  along  $K$  (red),  $K'$  (blue), and  $M$  (green) directions. (e) The geometry of the square lattice with lateral inversion symmetry breaking. (f)  $\Delta P_n$  for  $R$  (red) and  $L$  (blue) zigzaglike lattices with opposite symmetry.

appears at  $\sim 0.3$  T, as indicated by the blue arrow. The transmission signal  $S_{12}$  is larger than  $S_{21}$ , showing a nonreciprocity between the  $+k$  and  $-k$  SAW propagations. At the negative field side, the absorption peak appears at  $\sim -0.3$  T, with  $S_{12} < S_{21}$ , showing a nonreciprocity with an opposite sign. These absorption peaks and nonreciprocity show no difference in positive-to-negative and negative-to-positive field scans. Absorption peaks at low fields below 0.3 T show butterfly-shaped hysteresis and no nonreciprocity. This may be related to the magnetic resonance under the superlattice-induced anisotropy field in the sample (SM, Sec. 3) [31]. We hereafter focus on the high-field peaks. When the superlattice is rotated by  $180^\circ$ , the  $+k$  SAW is along the  $K'$  direction, and the  $-k$  SAW in the  $K$  direction. We name it the  $K'$ -oriented device ( $K'D$ ) [Fig. 2(b)]. Nonreciprocal absorption peaks appear in the same field but with  $S_{12} < S_{21}$  at positive and  $S_{12} > S_{21}$  at negative fields. The nonreciprocity signal takes an opposite sign in the  $K'D$  compared with the KD, revealing that the superlattice geometry governs the nonreciprocity.

As a control experiment, we rotated the superlattice by  $90^\circ$  so the SAW propagates along the  $M$  direction ( $M$ -oriented device, MD). In this configuration, the lattice preserves the mirror symmetry about the  $xz$  plane. The  $S_{12}$  and  $S_{21}$  are nearly identical, showing no noticeable nonreciprocity in this configuration. Honeycomb lattice with identical  $A$  and  $B$  sites also shows no nonreciprocity (SM, Sec. 4) [31]. The normalized nonreciprocal absorption  $\Delta P_n = (\Delta P_+ - \Delta P_-)/P$ , where  $\Delta P_\pm$  is the SAW absorbed power for  $\pm k$  (SM, Sec. 1) [31] and  $P$  is the transmission power at 0.6 T, is plotted in Fig. 2(d). Under the negative field,  $\Delta P_n$  is negative in KD (red), positive in K'D (blue), and close to zero in MD (green). The  $-k$  phonons in KD and the  $+k$  phonons in K'D are both in the  $K'$  valley, and both have stronger phonon scattering, represented by the more significant SAW attenuation. The  $K$  valley phonons, corresponding to the  $+k$  phonons in KD and the  $-k$  phonons in K'D, have a weaker phonon scattering. Nonreciprocity is absent in the  $M$  direction, which respects the mirror plane symmetry. When the magnetic field is opposite,  $\Delta P_n$  reverses its sign for both KD and K'D, showing that the  $+k$  phonons in KD and  $-k$  phonons in K'D attenuate more significantly due to a more pronounced phonon scattering in the  $K$  valley than the  $K'$  valley. The observed nonreciprocity thus originates from a valley-selective phonon-magnon scattering, where the magnetic field direction controls the selectivity over the  $K$  and  $K'$  valleys.

To further clarify the role of the honeycomb lattice in the observed nonreciprocity, we design a zigzaglike lattice with mirror symmetry breaking [Fig. 2(e)]. The  $L$  and  $R$  lattices have broken mirror symmetry about the  $xz$  plane, which allows the zigzaglike lattice to have nonreciprocity. However, as shown in Fig. 2(f),  $\Delta P_n$  in both  $R$  (red) and  $L$  (blue) lattices is more than 4 times smaller than the honeycomb lattice. One underlying reason is that the zigzaglike lattice has no valley degree of freedom since its Brillouin zone corners are all equivalent.  $\pm k$  SAW will excite the same phonon states at  $M$  in the square Brillouin zone, leading to identical phonon-magnon scattering. The nonreciprocity is then canceled when  $k$  is exactly located at  $M$ , and exists only with a broadened  $k$  distribution. We thus expect a small nonreciprocity regardless of the details of the zigzaglike structure, and conclude that the broken  $xz$  mirror symmetry is insufficient to generate large nonreciprocity. The sizable nonreciprocity observed in the honeycomb lattice benefits from the valley degrees of freedom.

To understand the role of magnetic structure on the valley-selective phonon-magnon scattering, we study the out-of-plane magnetic field angle dependence of the transmission in KD. The measurement geometry is shown in Fig. 3(a), where  $\theta_H$  is the magnetic field tilting angle and  $\theta$  is the angle between the magnetization and the  $z$  axis. Because of the easy-plane anisotropy of the Ni film, under moderate magnetic field,  $\theta$  can be significantly different

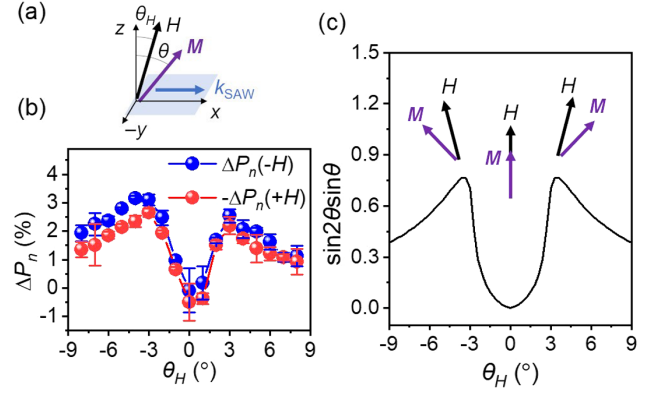


FIG. 3. (a) Schematic of the magnetization angle  $\theta$  under the external field  $H$  and the easy-plane anisotropy. (b) Peak absolute value of  $\Delta P_n$  as a function of the magnetic field tilting angle  $\theta_H$ . The blue and red data points correspond to negative and positive fields, respectively. (c) Calculated  $\sin 2\theta \sin \theta$  at resonance condition  $f_{\text{FMR}} = f_{\text{SAW}}$  as a function of  $\theta_H$ . Illustrations show the direction of magnetization  $M$  at resonance condition for  $\theta_H = 0^\circ, \pm 3^\circ$ .

from  $\theta_H$ . We focus on the  $\theta_H$  dependence in the  $xz$  plane to avoid additional nonreciprocity from the conventional mechanisms, generated by the  $y$  component of magnetization [27,32,41]. After scanning the magnetic field at each  $\theta_H$ , the peak value of  $\Delta P_n$  as a function of  $\theta_H$  is plotted in Fig. 3(b).  $\Delta P_n$  is almost zero at  $\theta_H = 0^\circ$  and nearly symmetric about  $\theta_H = 0^\circ$ . When the field is tilted away from  $\theta_H = 0^\circ$ ,  $\Delta P_n$  initially increases, peaks at approximately  $\pm 3^\circ$ , and then decreases gradually.

The predominant magnetic field-dependent SAW absorption mechanism in unpatterned Ni film is magnetoelastic coupling due to longitudinal strain  $\epsilon_{xx}$  [33,41]. The magnon-phonon coupling due to the longitudinal strain takes a maximum when the magnetization is directed at  $45^\circ$  from the SAW wave vector, and becomes zero when the magnetization is parallel or perpendicular to the wave vector [33,42]. Therefore, with  $\epsilon_{xx}$  only, the magnon-phonon coupling would be minimized at  $\theta = 0^\circ$  and peaked when  $\theta = 45^\circ$  at the resonance condition. Meanwhile, the valley phonons can excite rotating displacements in the  $xy$  plane [22], leading to an additional shear strain component  $\epsilon_{xy}$ , whose phase is shifted from  $\epsilon_{xx}$ . Assuming the dominant terms in magnetoelastic coupling come from these two strain components, one gets

$$\Delta P_n \propto b^2 L \sin 2\theta \sin \theta, \quad (1)$$

where  $b$  is the magnetoelastic coupling constant, and

$$L = \langle \epsilon_{xx}(d\epsilon_{xy}/dt) - \epsilon_{xy}(d\epsilon_{xx}/dt) \rangle, \quad (2)$$

with the angled bracket representing time averaging. The detailed derivation is given in SM, Sec. 4 [31].  $L$  represents

a circular polarization of the strain field. It is odd in frequency  $\omega$ , while any physical observable of classical wave should be even in  $\omega, k$ , so that it should also be odd in  $k$ , contributing to the nonreciprocity. Sign change in  $\theta$  results in the same  $\sin 2\theta \sin \theta$ , so that the nonreciprocity given by Eq. (1) is symmetric about  $\theta_H = 0^\circ$ . Equation (1) gives a maximum  $\Delta P_n$  at  $\theta = \pm 54.7^\circ$ , slightly off  $\pm 45^\circ$ .

To find the magnetization direction  $\theta$  at the resonance condition under a given  $\theta_H$ , we measured the saturation magnetic field in our superlattice using the anomalous Hall effect, and obtained saturation magnetization  $M_S \sim 2.8 \times 10^5$  A/m (Fig. S6) [31]. Based on a marcospin model, we calculate the magnetization direction  $\theta$  at which the ferromagnetic resonance (FMR) frequency  $f_{\text{FMR}}$  meets the SAW frequency  $f_{\text{SAW}}$ ; the detailed discussion is given in SM, Sec. 5 [31]. Then  $\sin 2\theta \sin \theta$  is plotted as a function of  $\theta_H$  in Fig. 3(c). The curve reproduces the key features of the experimental results in Fig. 3(b), including the dip at  $\theta_H = 0^\circ$ , the peak at  $\sim 3^\circ$ , and the gradual decrease when  $\theta_H$  becomes larger. The dip at  $\theta_H = 0^\circ$  is due to the fully out-of-plane magnetization  $\mathbf{M}$ , the peaks at  $\theta_H \sim \pm 3^\circ$  correspond to  $\theta = \pm 54.7^\circ$ , and when  $|\theta_H| > 3^\circ$ ,  $|\theta|$  gets greater than  $54.7^\circ$ , causing the gradual decrease in  $\sin 2\theta \sin \theta$ , as illustrated in Fig. 3(c). The good agreement between the calculated curve and the experimental results supports the magnetoelastic coupling as the primary magnon-phonon coupling mechanism in the valley-selective phonon-magnon scattering.

We finally study the nonreciprocal transmission spectra and analyze their relationship with the phonon bands. We focus on the peak condition for  $\Delta P_n$  at  $\pm 0.28$  T with  $\theta_H = 3^\circ$ , allowing us to use the ratio  $\eta = (\Delta P_+ - \Delta P_-) / (\Delta P_+ + \Delta P_-)$  as a sensible measure of nonreciprocity. Figure 4(a) displays  $\eta$  in KD at  $\pm 0.28$  T (blue and red points), together with the normalized transmission power  $P/P_{w/o}$  at 0.6 T (green curve), as a function of SAW frequency  $f$ . Here,  $P$  and  $P_{w/o}$  represent the transmission power with and without superlattice, respectively, detailed in SM, Sec. 1 [31].  $P/P_{w/o}$  has a dip at 1.815 GHz, characterizing the gap in the phonon frequency spectrum induced by the lattice. The evolution of  $\eta$  is closely related to this spectral gap. When  $f$  is far from the gap frequency of 1.815 GHz,  $\eta$  is small, but it changes dramatically across the gap. At  $\mu_0 H = -0.28$  T,  $\eta$  exhibits a negative value at  $f = 1.80$  GHz, changes its sign at the gap center at  $f = 1.815$  GHz, and reaches a peak at 1.82 GHz. The sign of  $\eta$  is reversed when  $\mu_0 H = 0.28$  T.

The strong correlation between the nonreciprocity and the gap shows that the former originated from the band structure of the superlattice. In the honeycomb lattice, the incident Rayleigh wave with wave vector  $\mathbf{k}$  near the  $K$  point is efficiently scattered into the hybridization of three Rayleigh waves with wave vector  $\mathbf{k}, \mathbf{k} - \mathbf{b}_1$ , and  $\mathbf{k} - \mathbf{b}_2$ , where  $\mathbf{b}_1, \mathbf{b}_2$  are the reciprocal lattice vectors [Fig. 4(b)]. Such hybridized phonon states can induce a local strain

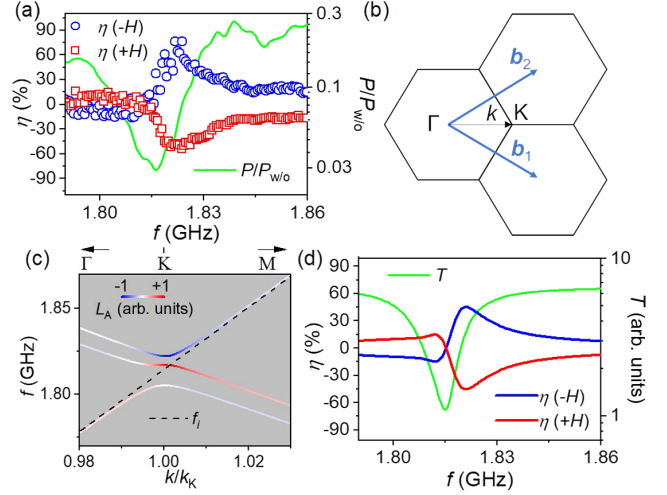


FIG. 4. (a) Nonreciprocity  $\eta = (\Delta P_+ - \Delta P_-) / (\Delta P_+ + \Delta P_-)$  at the peak position as a function of SAW frequency  $f$  at positive (red points) and negative (blue points) field. The green curve is the normalized transmission power  $P/P_{w/o}$  as a function of  $f$ . (b) Schematic of the Brillouin zones sharing the  $K$  point and the relevant reciprocal lattice vectors. (c) Phonon band dispersion in the plane-wave scattering model near  $K$  point. The red, blue, and white colors represent the positive, negative, and zero strain polarization  $L_A$  at site  $A$ , respectively. The wave vector at  $K$  is defined as  $k_K$ . The incident wave is represented by the dashed line. (d) Nonreciprocity  $\eta$  (blue and red) and the  $x$  component of energy flux  $T$  (green) as functions of  $k$  calculated from the elastic wave scattering model.

polarization  $L(\mathbf{r})$  [Eq. (2)]. While the averaged  $L$  itself vanishes [12,31], the  $A$  and  $B$  sites are surrounded by different magnetic environments, i.e., the phonons experience a periodically modulated magnon-phonon coupling, resulting in a nonreciprocity given by Eq. (1). At the same time, the scattering leads to interference and opens a gap. Both effects are characteristic to the perturbation of almost degenerate wave modes occurring at the Brillouin zone corners. Hence, the nonreciprocity is anticipated to reach a peak around the gap in the perturbed spectrum.

Based on elastic wave scattering models [34,35], phononic band dispersion, eigenmodes, and  $L(\mathbf{r})$  are computed, as detailed in SM, Sec. 6 [31]. We show  $L_A = L(\mathbf{r} = \mathbf{r}_A)$  at the high symmetry point  $A$  of each eigenmode together with the band dispersion in Fig. 4(c). The hybridization between  $\mathbf{k}, \mathbf{k} - \mathbf{b}_1$ , and  $\mathbf{k} - \mathbf{b}_2$  plane waves at  $k = k_K$  opens gaps, where  $k_K$  labels the wave vector at the  $K$  point. The hybridization also generates nonzero  $L_A$ . When  $k = k_K$ , the lowest band possesses nearly zero  $L_A$ , the middle has a positive  $L_A$ , and the highest a negative  $L_A$ . The hybridization decreases when  $k$  shifts from  $k_K$ , and  $L_A$  reduces. By time-reversal symmetry, the band structure at the  $K'$  valley is the same dispersion with the opposite  $L$ . The dashed line shows the dispersion of the incident wave, which couples to the eigenmodes and generates the strain polarization.

Figure 4(d) shows the theoretical nonreciprocity  $\eta$  (blue and red) and the  $x$  component of the phonon energy flux  $T$  (green) as a function of  $k$ , which qualitatively reproduce the tendency observed in the experiment [Fig. 4(a)]. For negative  $H$  and  $f$  below the gap, the incident wave is scattered into the lowest eigenmodes, which have positive  $L_A$ , resulting in negative nonreciprocity. Right above the gap, the incident wave couples to the highest mode, which has a large negative  $L_A$ , and the nonreciprocity reaches a maximum in the whole spectrum. Shifting frequency away from the gap leads to the coupling with eigenmodes with smaller  $L_A$ , and smaller nonreciprocity. For positive  $H$ , the nonreciprocity follows the same tendency with a reversed sign. The experiment and the calculation consistently show that in the valley-selective phonon-magnon scattering, the nonreciprocity originates from the strain polarization, enabled by the plane wave hybridization in the phononic crystal.

In summary, we observed valley-selective phonon-magnon scattering in magnetic honeycomb superlattices, which are phononic crystals with magnon-phonon coupling. The different phonon scatterings at  $K$  and  $K'$  valleys manifest themselves as nonreciprocal SAW transmission. The nonreciprocal absorption maintains a similar magnitude but changes sign when the superlattice symmetry is reversed. In zigzaglike lattices without valley degrees of freedom, nonreciprocal absorption becomes four times smaller, even with the inversion symmetry breaking. The nonreciprocal absorption is maximized when the magnetic field is directed at  $3^\circ$  from the  $z$  axis in the  $xz$  plane, which can be explained by a strain polarization coupled to the magnetization through the conventional magnetoelastic interaction. The nonreciprocity spectrum shows a peak near the transmission gap, matching with the distribution of the strain polarization in the phonon bands. The valleys, encoding the superlattice geometry and symmetry, are the key to induce the nonreciprocity, whereby the observed effect can be termed a valley-selective phonon-magnon scattering. Different from the edge modes, our approach provides a way to apply valley phonon in the bulk transport regime. It demonstrates the periodically modulated magnon-phonon coupling as a new tool for controlling the valley phonon transport.

We thank Yoichi Nii, Konstantin Bliokh, Lei Han, Huiping Xu, and Joseph Barker for fruitful discussions and helpful comments. This work is supported by JSPS KAKENHI 19H05629. K. Y. acknowledges support from JST PRESTO Grant No. JPMJPR20LB, Japan and JSPS KAKENHI (No. 21K13886), and Y. O. from The LANEF Chair of Excellence, QSPIN project, at University Grenoble Alpes. S. M. is financially supported by JST CREST (No. JPMJCR19J4, No. JPMJCR1874, and No. JPMJCR20C1) and JSPS KAKENHI (No. 20H01865) from MEXT Japan. L. L. would like to thank JSPS for support through “Research Program for Young Scientists” (No. 23KJ0778). Y. H. acknowledges support from RIKEN Junior Research Associate Program.

\*jorgeluis.pueblanunez@riken.jp

†yotani@issp.u-tokyo.ac.jp

- [1] Y. Cao, V. Fatemi, S. Fang, K. Watanabe, T. Taniguchi, E. Kaxiras, and P. Jarillo-Herrero, Unconventional superconductivity in magic-angle graphene superlattices, *Nature (London)* **556**, 43 (2018).
- [2] M. Yankowitz, S. Chen, H. Polshyn, Y. Zhang, K. Watanabe, T. Taniguchi, D. Graf, A. F. Young, and C. R. Dean, Tuning superconductivity in twisted bilayer graphene, *Science* **363**, 1059 (2019).
- [3] A. L. Sharpe, E. J. Fox, A. W. Barnard, J. Finney, K. Watanabe, T. Taniguchi, M. A. Kastner, and D. Goldhaber-Gordon, Emergent ferromagnetism near three-quarters filling in twisted bilayer graphene, *Science* **365**, 605 (2019).
- [4] M. Serlin, C. L. Tschirhart, H. Polshyn, Y. Zhang, J. Zhu, K. Watanabe, T. Taniguchi, L. Balents, and A. F. Young, Intrinsic quantized anomalous Hall effect in a moiré heterostructure, *Science* **367**, 900 (2020).
- [5] J. Holanda, D. S. Maior, A. Azevedo, and S. M. Rezende, Detecting the phonon spin in magnon-phonon conversion experiments, *Nat. Phys.* **14**, 500 (2018).
- [6] J. Puebla, Y. Hwang, S. Maekawa, and Y. Otani, Perspectives on spintronics with surface acoustic waves, *Appl. Phys. Lett.* **120**, 220502 (2022).
- [7] Y. Li, C. Zhao, W. Zhang, A. Hoffmann, and V. Novosad, Advances in coherent coupling between magnons and acoustic phonons, *APL Mater.* **9**, 060902 (2021).
- [8] Y. Kurimune, M. Matsuo, and Y. Nozaki, Observation of Gyromagnetic Spin Wave Resonance in NiFe Films, *Phys. Rev. Lett.* **124**, 217205 (2020).
- [9] S. Y. Yu, X. C. Sun, X. Ni, Q. Wang, X. J. Yan, C. He, X. P. Liu, L. Feng, M. H. Lu, and Y. F. Chen, Surface phononic graphene, *Nat. Mater.* **15**, 1243 (2016).
- [10] B. Z. Xia, T. T. Liu, G. L. Huang, H. Q. Dai, J. R. Jiao, X. G. Zang, D. J. Yu, S. J. Zheng, and J. Liu, Topological phononic insulator with robust pseudospin-dependent transport, *Phys. Rev. B* **96**, 094106 (2017).
- [11] Z. Tian, C. Shen, J. Li, E. Reit, H. Bachman, J. E. S. Socolar, S. A. Cummer, and T. Jun Huang, Dispersion tuning and route reconfiguration of acoustic waves in valley topological phononic crystals, *Nat. Commun.* **11**, 762 (2020).
- [12] J. Lu, C. Qiu, M. Ke, and Z. Liu, Valley Vortex States in Sonic Crystals, *Phys. Rev. Lett.* **116**, 093901 (2016).
- [13] P. Pirro, V. I. Vasyuchka, A. A. Serga, and B. Hillebrands, Advances in coherent magnonics, *Nat. Rev. Mater.* **6**, 1114 (2021).
- [14] A. V. Chumak, V. I. Vasyuchka, A. A. Serga, M. P. Kostylev, V. S. Tiberkevich, and B. Hillebrands, Storage-Recovery Phenomenon in Magnonic Crystal, *Phys. Rev. Lett.* **108**, 257207 (2012).
- [15] D. Richardson, B. A. Kalinikos, L. D. Carr, and M. Wu, Spontaneous Exact Spin-Wave Fractals in Magnonic Crystals, *Phys. Rev. Lett.* **121**, 107204 (2018).
- [16] Z. Hu, L. Fu, and L. Liu, Tunable Magnonic Chern Bands and Chiral Spin Currents in Magnetic Multilayers, *Phys. Rev. Lett.* **128**, 217201 (2022).
- [17] H. Zeng, J. Dai, W. Yao, D. Xiao, and X. Cui, Valley polarization in MoS<sub>2</sub> monolayers by optical pumping, *Nat. Nanotechnol.* **7**, 490 (2012).

- [18] J. R. Schaibley, H. Yu, G. Clark, P. Rivera, J. S. Ross, K. L. Seyler, W. Yao, and X. Xu, Valleytronics in 2D materials, *Nat. Rev. Mater.* **1**, 16055 (2016).
- [19] M. Yan, J. Lu, F. Li, W. Deng, X. Huang, J. Ma, and Z. Liu, On-chip valley topological materials for elastic wave manipulation, *Nat. Mater.* **17**, 993 (2018).
- [20] Q. Zhang *et al.*, Gigahertz topological valley Hall effect in nanoelectromechanical phononic crystals, *Nat. Electron.* **5**, 157 (2022).
- [21] C. He, X. Ni, H. Ge, X. C. Sun, Y. Bin Chen, M. H. Lu, X. P. Liu, and Y. F. Chen, Acoustic topological insulator and robust one-way sound transport, *Nat. Phys.* **12**, 1124 (2016).
- [22] Y. Nii and Y. Onose, Imaging an Acoustic Topological Edge Mode on a Patterned Substrate with Microwave Impedance Microscopy, *Phys. Rev. Appl.* **19**, 014001 (2023).
- [23] J. Zhao, C. Yang, W. Yuan, D. Zhang, Y. Long, Y. Pan, H. Chen, Z. Zhong, and J. Ren, Elastic Valley Spin Controlled Chiral Coupling in Topological Valley Phononic Crystals, *Phys. Rev. Lett.* **129**, 275501 (2022).
- [24] E. Thingstad, A. Kamra, A. Brataas, and A. Sudbø, Chiral Phonon Transport Induced by Topological Magnons, *Phys. Rev. Lett.* **122**, 107201 (2019).
- [25] G. Go, S. K. Kim, and K. J. Lee, Topological Magnon-Phonon Hybrid Excitations in Two-Dimensional Ferromagnets with Tunable Chern Numbers, *Phys. Rev. Lett.* **123**, 237207 (2019).
- [26] S. Zhang, G. Go, K. J. Lee, and S. K. Kim, SU(3) Topology of Magnon-Phonon Hybridization in 2D Antiferromagnets, *Phys. Rev. Lett.* **124**, 147204 (2020).
- [27] M. Küss, M. Heigl, L. Flacke, A. Hörner, M. Weiler, M. Albrecht, and A. Wixforth, Nonreciprocal Dzyaloshinskii-Moriya Magnetoacoustic Waves, *Phys. Rev. Lett.* **125**, 217203 (2020).
- [28] M. Xu, K. Yamamoto, J. Puebla, K. Baumgaertl, B. Rana, K. Miura, H. Takahashi, D. Grundler, S. Maekawa, and Y. Otani, Nonreciprocal surface acoustic wave propagation via magneto-rotation coupling, *Sci. Adv.* **6**, abb1724 (2020).
- [29] Y. Hwang, J. Puebla, K. Kondou, and Y. Otani, Voltage signals caused by surface acoustic wave driven ferromagnetic resonance under out-of-plane external fields, *Adv. Mater. Interfaces* **9**, 2201432 (2022).
- [30] C. Chen, S. Fu, L. Han, R. Su, P. Liu, R. Chen, W. Zhu, L. Liao, F. Pan, and C. Song, Energy Harvest in ferromagnet-embedded surface acoustic wave devices, *Adv. Electron. Mater.* **8**, 2200593 (2022).
- [31] See Supplemental Material at <http://link.aps.org/supplemental/10.1103/PhysRevLett.131.176701> for sample layout, and transmission spectra, influence of the substrate orientation, in-plane scan, and low field absorption, SAW transmission in honeycomb lattice with identical A and B sites, derivation of the theoretical nonreciprocal power, estimation of the magnetization tilting angle, elastic wave scattering model, and theoretical nonreciprocity, with Refs. [22,25,32–40].
- [32] S. Tateno, Y. Nozaki, and Y. Nozaki, Highly Nonreciprocal Spin Waves Excited by Magnetoelastic Coupling in a Ni/Si Bilayer, *Phys. Rev. Appl.* **13**, 034074 (2020).
- [33] M. Xu, J. Puebla, F. Auvray, B. Rana, K. Kondou, and Y. Otani, Inverse Edelstein effect induced by magnon-phonon coupling, *Phys. Rev. B* **97**, 180301(R) (2018).
- [34] M. S. Kushwaha, P. Halevi, G. Martínez, L. Dobrzynski, and B. Djafari-Rouhani, Theory of acoustic band structure of periodic elastic composites, *Phys. Rev. B* **49**, 2313 (1994).
- [35] E. N. Economou and M. Sigalas, Stop bands for elastic waves in periodic composite materials, *J. Acoust. Soc. Am.* **94**, 1734 (1994).
- [36] M. Hu and F. Li Duan, Design, fabrication, and characterization of SAW devices on LiNbO<sub>3</sub> bulk, and ZnO thin film substrates, *Solid State Electron.* **150**, 28 (2018).
- [37] V. S. Bhat, F. Heimbach, I. Stasinopoulos, and D. Grundler, Magnetization dynamics of topological defects and the spin solid in a kagome artificial spin ice, *Phys. Rev. B* **93**, 140401(R) (2016).
- [38] Q. Li, S. Xiong, L. Chen, K. Zhou, R. Xiang, H. Li, Z. Gao, R. Liu, and Y. Du, Spin-wave dynamics in an artificial kagome spin ice, *Chin. Phys. Lett.* **38**, 047501 (2021).
- [39] R. Su *et al.*, Wideband and low-loss surface acoustic wave filter based on 15° YX-LiNbO<sub>3</sub>/SiO<sub>2</sub>/Si structure, *IEEE Electron Device Lett.* **42**, 438 (2021).
- [40] K. Yamamoto, M. Xu, J. Puebla, Y. Otani, and S. Maekawa, Interaction between surface acoustic waves and spin waves in a ferromagnetic thin film, *J. Magn. Magn. Mater.* **545**, 168672 (2022).
- [41] R. Sasaki, Y. Nii, Y. Iguchi, and Y. Onose, Nonreciprocal propagation of surface acoustic wave in Ni/LiNbO<sub>3</sub>, *Phys. Rev. B* **95**, 020407(R) (2017).
- [42] M. Weiler, H. Huebl, F. S. Goerg, F. D. Czeschka, R. Gross, and S. T. B. Goennenwein, Spin Pumping with Coherent Elastic Waves, *Phys. Rev. Lett.* **108**, 176601 (2012).